Nanoscale

ROYAL SOCIETY OF CHEMISTRY

PAPER

View Article Online
View Journal | View Issue

Cite this: *Nanoscale*, 2025, **17**, 20327

Conductance modulation in graphene/antiferromagnet van der Waals heterostructures induced by magnetic order

Adrián García-Martín,[a] Rocío Sánchez-de-Armas,[b] Sara Gullace,[c] Esther Calle,[d] Lucía Martín-Pérez,[c] Nicolás Montenegro-Pohlhammer,[b] Miriam Jaafar,[d] José Sanchez Costa,[c,e] Carmen J. Calzado *[b] and Enrique Burzurí *[a,f]

Received 13th June 2025,
Accepted 18th August 2025

DOI: 10.1039/d5nr02538a

rsc.li/nanoscale

Two-dimensional (2D) van der Waals (vdW) antiferromagnets (AFMs) have emerged as promising candidates for spintronic applications due to their fast spin dynamics and robustness against external magnetic perturbations. However, their intrinsically low electrical conductivity challenges their integration into electronic devices. A possible path to overcome this limitation is to form vdW heterostructures with highly conductive materials such as graphene, which can sensitively respond to interfacial magnetic interactions. Such an interplay is, however, far from being understood. In this work, we investigate vdW heterostructures composed of single-layer graphene and the antiferromagnet $FePS_3$ (FEPS). Electron transport measurements in a field-effect transistor geometry reveal a sharp change in graphene resistance precisely at the Néel temperature of FEPS. Temperature-dependent Raman spectroscopy and gate-dependent transport suggest a distinct interfacial charge transfer driven by the antiferromagnetic ordering. Density functional theory (DFT) calculations support this mechanism, showing a significant modulation of charge transfer across the interface linked to the magnetic phase. These findings unveil a strong interplay between magnetism and electron transport in 2D vdW heterostructures and pave the way toward integrating antiferromagnetic vdW materials into future electronic and spintronic technologies.

Introduction

Magnetism in the two-dimensional limit has been a long-time unexplored field due to the scarcity of true 2D magnetic materials and the existence of magnetic order contingent on the presence of magnetic anisotropy in the material.[1] The available candidates were limited to only a handful of quasi-2D systems.[2] This stalemate situation drastically changed with the ability to exfoliate vdW crystals into monoatomic-thick, truly-2D layers. vdW crystals are made of covalently bonded 2D layers weakly held together into three-dimensional bulky crystals by vdW interactions. The first vdW crystals displaying magnetic order in the monolayer limit were the Ising antiferromagnet FEPS and the ferromagnetic CrI_3 and $Cr_2Ge_2Te_6$.[3–6] These findings triggered a race to gain a deeper understanding of magnetism in the 2D limit. In a few years, the field has witnessed the electric control of the magnetism in monolayers, the tuning of magnetic interactions by the number of layers and/or stacking geometry, the emergence of magnetic textures like skyrmions and Moiré magnetism in twisted magnetic bilayers, all these effects being observed in ferromagnets.[5,7–11]

Among 2D magnetic materials, vdW AFMs, typically overshadowed by 2D vdW ferromagnets, are becoming increasingly interesting despite their vanishing net magnetization. In antiferromagnetic materials, the magnetic excitations, known as magnons, can propagate with lower damping than in ferromagnets, making AFMs suitable for spintronics. Besides, spin switching in AFMs is mediated by these same magnon excitations, typically in the THz range. AFMs thus show faster spin dynamics when compared with ferromagnets operating in the

[a]*Dpto. Física de la Materia Condensada, Universidad Autónoma de Madrid, c/ Francisco Tomás y Valiente 7, 28049 Madrid, Spain. E-mail: enrique.burzuri@uam.es*
[b]*Dpto. Química Física, Universidad de Sevilla, c/Profesor García González, s/n, 41012 Sevilla, Spain. E-mail: calzado@us.es*
[c]*IMDEA Nanociencia C/Faraday 9, Ciudad Universitaria de Cantoblanco, 28049 Madrid, Spain*
[d]*Instituto de Ciencia de Materiales de Madrid (ICMM–CSIC), c/Sor Juana Inés de la Cruz 3, 28049 Madrid, Spain*
[e]*Unidad de Nanomateriales Avanzados, IMDEA-Nanociencia, Unidad Asociada al CSIC por el ICMM, c/Faraday 9, 28049 Madrid, Spain*
[f]*Condensed Matter Physics Center (IFIMAC) and Instituto Universitario de Ciencia de Materiales "Nicolás Cabrera" (INC), Universidad Autónoma de Madrid, c/Francisco Tomás y Valiente 7, 28049 Madrid, Spain*

GHz range.[12] Moreover, the lack of net magnetization makes AFMs robust against external magnetic perturbations, ensuring also a null stray field for vanishing crosstalk between adjacent bits, important characteristics for spintronic device stabilization and high-density integration.[12,13] Finally, 2D AFMs are firm candidates to host exotic states of matter like quantum spin liquids, in specific lattice arrangements.[14] Beyond these intrinsic properties, vdW magnetic 2D layers present yet another unique property: the ability to easily form heterostructures by stacking two different vdW atomic layers on top of each other.[15] Such combination may allow providing 2D magnets with properties typically not present in the isolated materials, like electrical and thermal conductivity or photoresponsivity, which could in turn facilitate the integration of the 2D magnets into quantum and spintronics devices. However, a significant limitation hindering the device integration of 2D antiferromagnets lies in the inherent difficulty of probing their antiferromagnetic state.[16]

In this regard, graphene seems to be the most natural candidate to form vdW heterostructures with 2D magnets. Its high carrier mobility, long spin coherence length, and tunable band structure make graphene a potential platform to translate the magnetism in the magnetic sublayer into electrical signals. Besides, graphene may act beyond being a passive detector. Instead, the magnetic proximity effect induced by the AFM layer on graphene is predicted to produce exotic physics. For example, magnetic proximity effect has induced large spin splitting in graphene by the CrSe AFM and the $MnPS_3$ AFM in heterostructures.[16,17] This effect led in some cases to the observation of quantum anomalous Hall effect or exotic quantum Hall effect, that could lead to a control over the electronic states *via* interfacial charge coupling.[16,18]

The interplay between graphene and the 2D AFM is, however, non-trivial and far from being understood in the heterostructure. It heavily depends on the interfacial coupling between the layers that is known to be rather inhomogeneous across the contact surface.[19] Pristine layers are difficult to obtain and diverse factors such as defects, surface roughness or source impurities can significantly affect the overall device characteristics and performance.[20,21]

Probably for this reason, several experimental works show a variety of results where the role of the AFM magnetic phase on graphene's electron transport remains unclear. Wu *et al*. show that the AFM transition is accompanied by a kink in the graphene resistivity concomitant with spin-splitting and magnetization of graphene.[17] Other reports on graphene/AFM heterostructures show instead very weak variations of the resistivity at the antiferromagnet Néel temperature. Instead, they find that the spin-dependent hybridization of the materials occurs irrespectively of the magnetic phase or is related to inhomogeneous charge transfer at the contact surface.[19,22]

Some others show variations in the resistivity well below the Néel temperature, these being associated with Kondo physics of magnetic impurities and therefore not related to the magnetic order.[23] A deeper understanding of the interplay between the electronic and magnetic properties of graphene and the 2D magnet in the heterostructure seems necessary and could pave the way for tunable spintronic devices, including low-power magnetic memory elements and spin-based logic components. In this work, we focus on vdW heterostructures conformed by graphene and the layered transition-metal phosphorus trichalcogenide $FePS_3$ (hereafter FEPS). FEPS is a vdW out-of-plane Ising antiferromagnet below Néel temperature (118 K) that preserves the AFM phase down to the monolayer limit.[3] See Fig. 1a for an atomistic representation of the heterostructure. Furthermore, FEPS is stable in ambient conditions and has lately shown intriguing properties like strong magnon–phonon coupling and terahertz field-induced metastable magnetization.[24–26]

We investigate electron transport in the graphene/FEPS heterostructure in a field-effect transistor (FET) geometry. We show that the magnetic transition in FEPS triggers an abrupt increment in graphene's resistance right at the Néel temperature. Interestingly, the change in resistance is concomitant with a large energy shift of the charge neutrality point in graphene, observed for the first time in variable gate measurements. Thus, our results point to a significant modulation of charge transfer across the interface linked to the magnetic phase in FEPS. These findings are supported by temperature-dependent Raman measurements and DFT calculations. The latter shows that electron charge transfer from graphene to FEPS is reduced in the AFM phase, supporting the larger resistance and the shift of the Dirac cone to more negative values observed in electron transport measurements.

Results and discussion

The magnetic structure of FEPS consists of a 2D honeycomb lattice of Fe ions (S = 2) coupled *via* superexchange interactions. The magnetic ground state is predicted to be a zigzag out-of-plane Ising antiferromagnet.[28] Fig. 1a and b show an atomistic model of the target $FePS_3$/chemical vapor deposited (CVD) graphene field-effect transistor heterostructure, hereafter FEPS/GFET, and a schematic view of the electrical circuit employed for the electron transport measurements. The devices are prepared by a dry transfer technique. Exfoliated FEPS flakes are initially obtained by repeated peeling of the bulk material with a piece of Nitto tape. Thereafter, the flakes are further exfoliated onto a piece of viscoelastic polydimethylsiloxane (PDMS) silicone polymer. The PDMS seal is mounted in a transfer station equipped with an optical microscope and a set of micromanipulators. The colour or optical reflectance of the different flakes of vdW materials in the PDMS can be non-trivially associated with their thickness.[29,30] The PDMS stamp area containing the selected flake is gently placed onto the CVDG window of a commercial CVDG FET. By carefully peeling off the PDMS seal, the FEPS stays adhered to the CVDG forming the FEPS/GFET heterostructure. See Fig. S1 in the SI for a summary of the fabrication process. Fig. 1c shows an optical image of a representative FEPS/GFET (device A). The underlying SiO_2 (90 nm) and Si substrate (675 μm) are used as

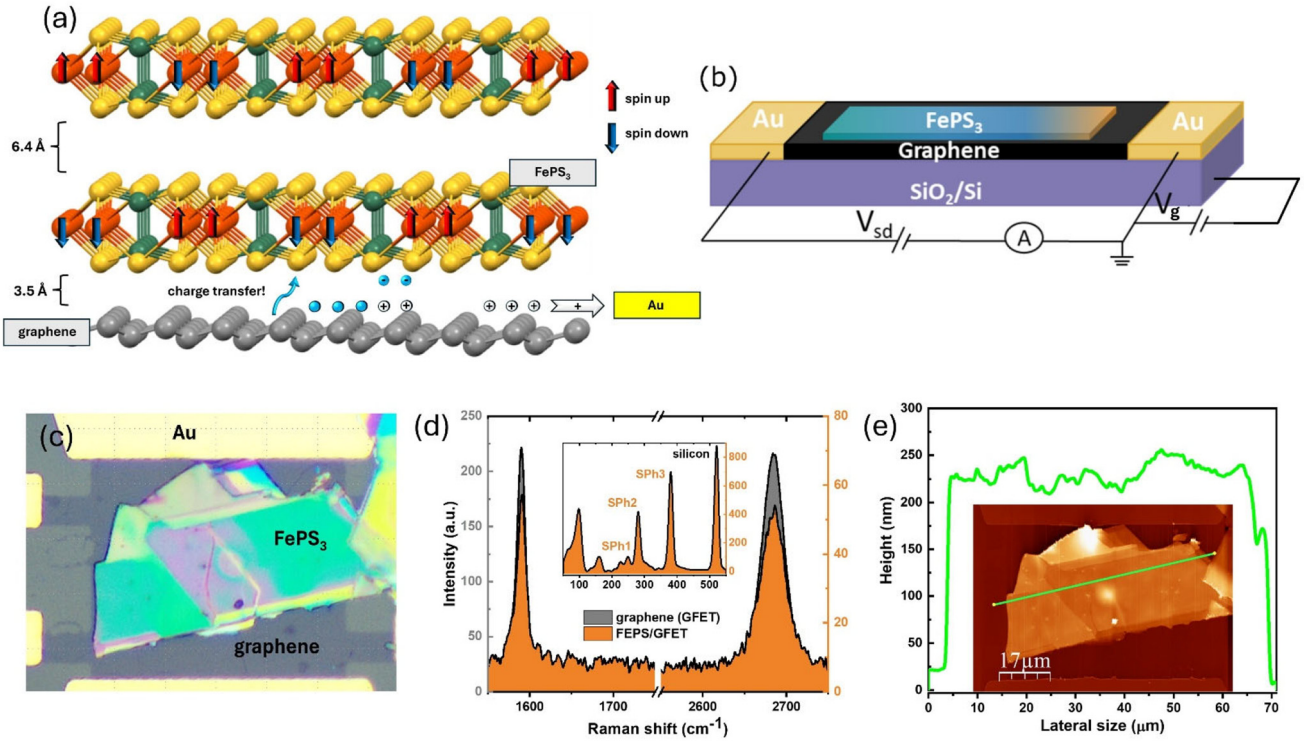

Fig. 1 (a) Atomistic representation of a FEPS/GFET heterostructure lateral view. Interlayer FEPS distance and DFT calculated distance between graphene and FEPS are also included.[4] (b) Schematics of the field effect transistor (FET) geometry used for the electron transport measurements in the heterostructure. (c) Optical image of a FEPS flake placed on top of a graphene FET; the FEPS/GFET (device A). (d) Raman spectra showing the intensity (I) of the G (I_G) and 2D (I_{2D}) main graphene bands measured on FEPS/GFET (device A, orange) and pristine GFET (gray) at room temperature. Inset: FEPS characteristic Raman bands.[27] (e) SFM height profile along the $FePS_3$ flake stamped onto the GFET (device A). Inset: topography SFM image of the heterostructure based device A.

gate dielectric and gate electrode, respectively. Exfoliation and transfer are performed in ambient conditions, as FEPS is described to be stable in air for long periods of time.[24]

The topography of the device and thickness of the FEPS flake are probed by Scanning Force Microscopy (SFM). An SFM image of the FEPS/GFET (device A) is shown in the inset of Fig. 1e. The height profile corresponding to the green line is shown in the main figure. The average thickness of the selected flake is 220 nm and is therefore far from the 2D limit of the underlying graphene monolayer. Nevertheless, large-area FEPS flakes are prioritized over thinner flakes to maximize the coverage area of the graphene FET, as the interests here mainly lie on the interfacial interaction between both vdW materials. This is common practice in the AFM/graphene heterostructures literature where the results do not seem to depend on the magnetic layer thickness.[4,17,21] Moreover, the interlayer spacing in FEPS (~6.4 Å) is larger than the predicted distance between the graphene monolayer and the first adjacent FEPS layer (~3.5 Å), as shown later by DFT calculations.[4]

Raman spectroscopy on device A provides information on its lattice structure and electronic properties after the formation of the FEPS/GFET heterostructure. Fig. 1d shows that pristine GFETs exhibit the typical G and 2D bands (grey). The initial intensity ratio, I_{2D}/I_G, of around 0.97 indicates that the starting graphene is intrinsically heavily doped, a phenomenon that has been usually ascribed to the presence of impurities from the CVD graphene production or the fabrication of the devices and is typically observed for graphene and other carbon allotropes-based FET.[31,32] Fig. 1d also shows the high and low energy Raman spectra for the FEPS/GFET heterostructure measured in ambient conditions (orange). Graphene G and 2D bands are clearly visible even below the $FePS_3$ flake. The ratio I_{2D}/I_G in the heterostructure is around 0.98, which indicates no major changes in graphene doping when the heterostructure is formed.[33] No significant shift is observed either in ω_{2D} when comparing GFET (2684 cm^{-1}) and FEPS/GFET (2686 cm^{-1}). Besides, the absence of the D band, typically related to disruptions of the sp^2 hybridization in the honeycomb layer, shows that the deposition of the antiferromagnetic material does not induce defects in the graphene structure. Finally, the low frequency range is dominated by the characteristic FEPS bands (see Fig. 1d inset).[27]

Temperature-dependent Raman spectroscopy has been performed on the same devices. Fig. 2a and b show the Raman spectra measured in pristine GFET and FEPS/GFET device A at different temperatures. All the curves in Fig. 2 are the result of averaging 8 different measurements for each device and temperature. By cooling to 90 K, ω_{2D} blue shifts to 2693 cm^{-1} ($\Delta\omega$ =

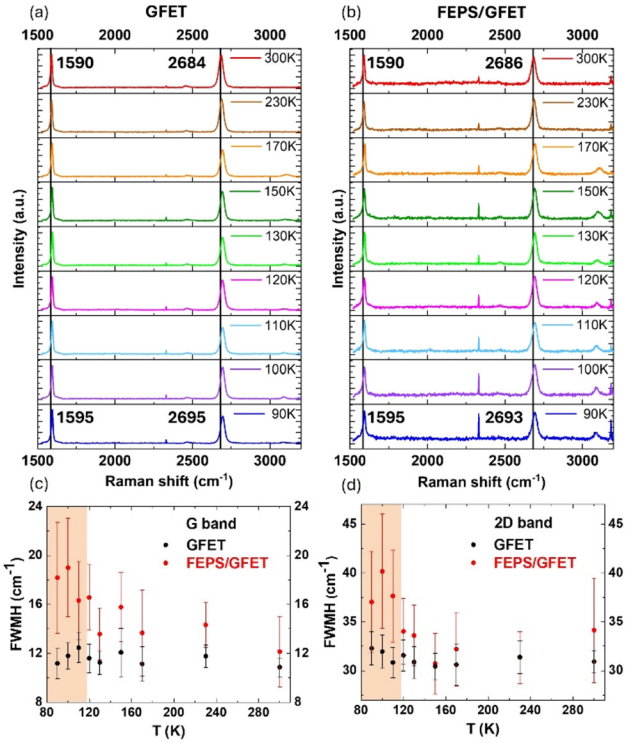

Fig. 2 (a and b) Raman spectra measured on (a) pristine GFET and (b) FEPS/GFET (device A) at different temperatures from room temperature down to 90 K. Straight black lines are a visual guide to show the shift of 2D and G bands in graphene. (c and d) Full Width at Half Maximum (FWHM) of (c) the G and (d) 2D bands as a function of temperature obtained for pristine GFET (black points) and FEPS/GFET (red points).

7 cm^{-1}) in the FEPS/GFET suggesting a minor increment of the carrier density when the temperature decreases. See also Fig. S2 in the SI. The same behavior is observed in the GFET (ω_{2D} (90 K) = 2695 cm^{-1}, $\Delta\omega$ = 11 cm^{-1}) pointing to an intrinsic variation in graphene not related to the presence of the FEPS flake. A similar although weaker shift is observed for the G peak position, being ω_G less sensitive to temperature (Fig. 2a and b).[34] These results may suggest that the flake does not alter graphene intrinsic electronic behavior.

No abrupt change in the graphene charge carrier concentration seems therefore to occur at the Néel temperature. Interestingly, a different picture emerges when analysing the full width at half maximum of the G and 2D peaks ($FWHM_G$, $FWHM_{2D}$), shown in Fig. 2c and d, respectively.[33] As seen in Fig. 2c, the $FWHM_G$ in the pristine GFET remains essentially constant at around 12 cm^{-1} throughout the entire investigated temperature range. This behavior is consistent with both theoretical and experimental reports on single layer graphene.[35] Constant values of $FWHM_G$ can be attributed to weak phonon anharmonicity and electron–phonon coupling in the studied temperature range.[35,36] In contrast, the $FWHM_G$ in the FEPS/GFET starts to increase near the FEPS Néel temperature. It has been reported that $FWHM_G$ decreases with increasing absolute values of the Fermi energy, due to the blockage of phonon decay into electron–hole pairs governed by the Pauli exclusion principle.[37] Therefore, the observed broadening of the G band in the FEPS/GFET heterostructure may be ascribed to a Fermi level reduction that comes hand in hand with a softening of the p-doping. Similarly, the observed increase in $FWHM_{2D}$ can be attributed to charge doping, which is coherent with the expected reduction of the p-type doping described for the G band.[38]

The Néel transition in FEPS seems therefore associated with a distinct charge transfer between FEPS and graphene. Note that the error bars for the heterostructure are larger than those of the pristine GFET. This is due to the greater data dispersion in the heterostructure. This variability is caused by the non-uniform coupling of the FEPS flake and the graphene monolayer, as seen in the individual Raman spectra shown in Table S1 in the SI. See error bars calculation in the Experimental section.

A deeper insight into the electronic properties of the FEPS/GFET can be obtained in temperature-dependent electron transport measurements. Note that charge carriers are expected to flow predominately through the graphene layer (see Fig. 1b) since graphene resistivity is at least 2 orders of magnitude lower than in FEPS.[39,40] Fig. 3a shows the current (I) measured as a function of the temperature (T) at a fixed bias voltage V = 1 V between source and drain electrodes on device B. The pristine GFET (that is, before stamping the FEPS) is also measured as a reference. The curves are normalized to the highest temperature value to facilitate direct comparison. See raw curves in Fig. S3 in the SI. Both FEPS/GFET and pristine GFET show a moderate and monotonic decrease in the current as the temperature is lowered from room temperature. Interestingly, a sharp decrease ($\Delta I \sim 13\%$) of the current in FEPS/CVDG is observed below 120 K that is not present in the pristine GFET ($\Delta I \sim 2\%$).

This critical temperature roughly matches the Néel temperature (118 K) for the antiferromagnetic transition in the FEPS pristine material.[41] Further compelling evidence can be found when comparing the temperature-dependent electrical current through graphene with the magnetic susceptibility measured on bulk FEPS (blue line in Fig. 3a). The drop in susceptibility, signature of the transition to an antiferromagnetic order in FEPS, quantitatively matches the drop on electric current in graphene. This measurement shows that the sharp increment in the electrical resistance in graphene is unambiguously triggered by the antiferromagnetic order in the FEPS flake.

Fig. S4 in the SI shows an additional FEPS/GFET heterostructure (device A) showing the same drop in conductance at the Néel temperature. The sharp jump observed in Fig. 3a at the lowest temperature is not observed and therefore is probably due to a thermalization issue in this particular measurement.

In total, 5 out of 7 measured devices shows a similar shift in resistance at the Néel temperature. Despite evidencing a big dispersion of the $FWHM_G$ data in the Raman measurements, the electrical properties of graphene in device A are significantly influenced by the FEPS magnetic ordering.

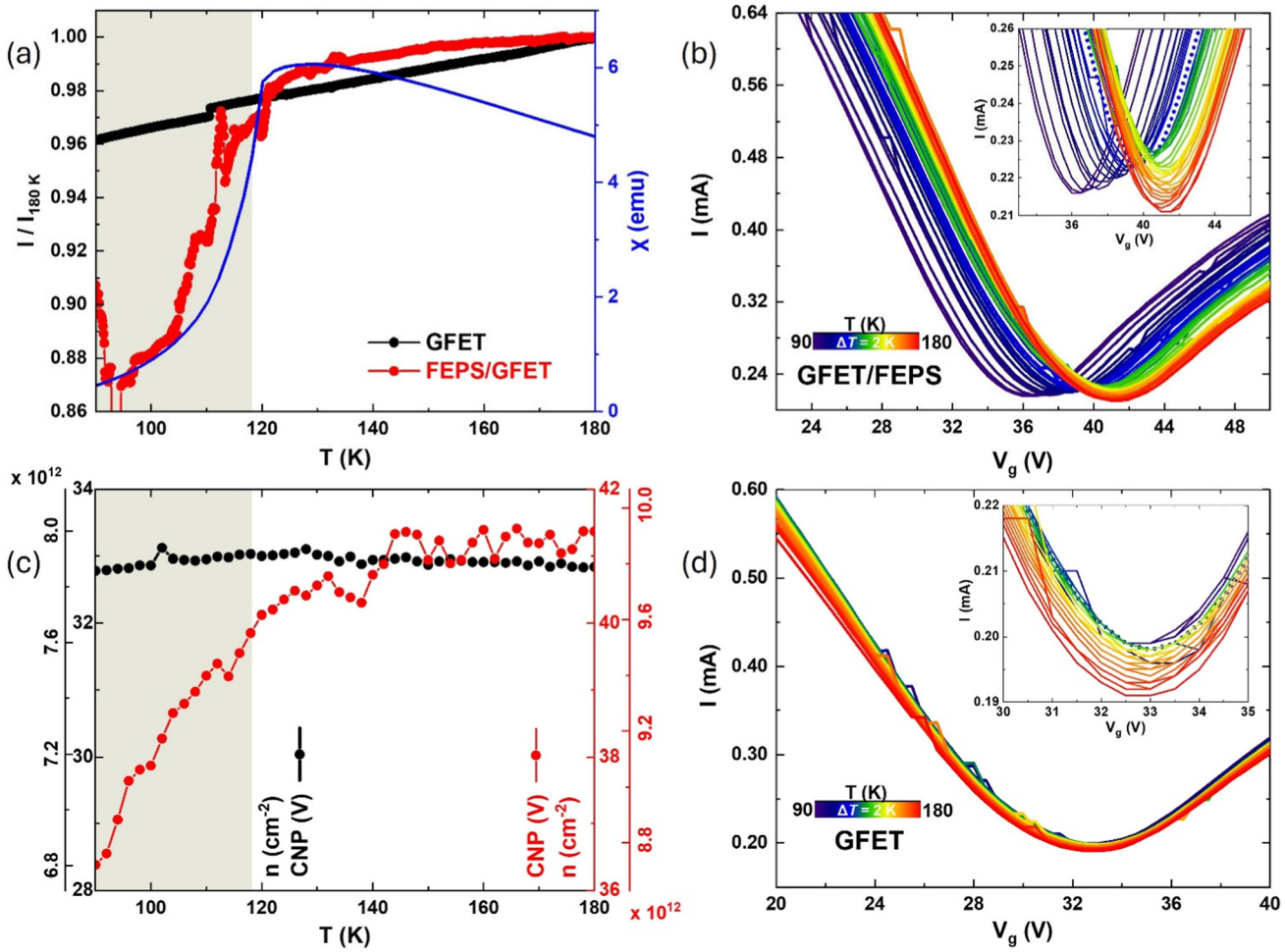

Fig. 3 Electrical characterization of a FEPS/GFET (device B). (a) Drain–source current I as a function of temperature T measured on a pristine GFET (black dots) and a FEPS/GFET (device B, red dots) for a fixed bias voltage of 1 V. The curves are normalized to the highest temperature value to facilitate direct comparison. A sharp drop in current is observed in the FEPS/GFET right at the Néel temperature, as clearly seen when comparing the magnetic susceptibility of bulk FEPS (blue line). The coloured background marks the bulk FEPS antiferromagnetic state. (b) Gate traces measured at different temperatures (from 90 K to 180 K with a 2 K step) for FEPS/GFET (device B). The bias is set to 1 V. Insets: zoom in on the charge neutrality point (CNP). The gate curve corresponding to Néel temperature is shown as a dotted line. (c) CNP and associated residual carrier density n at CNP as a function of temperature for GFET (black dots) and FEPS/GFET (red dots) obtained from (b and d). (d) Gate traces measured at different temperatures (from 90 K to 180 K with a 2 K step) for pristine GFET.

The lack of response in some devices may be attributed to inhomogeneous contact and a weaker interlayer coupling between FEPS and graphene in those specific devices.[17]

Similar but subtler variations in resistance right at the Néel temperature have been observed for $RuCl_3$ and CrSe-based AFM/graphene heterostructures.[17,19] In these examples, the Néel temperature is, however, close to the lower-limit measurement, and no conclusive analysis of the resistance change could be obtained. On the other hand, AFM/graphene heterostructures in the literature based on the same FEPS or the relatively similar $MnPSe_3$ do not show any significant variation of the resistance in graphene at the Néel temperature. The former may be due to an inhomogeneous weaker coupling between layers, as described by Yi *et al.*[23,27] The latter may be due to a different nature of the magnetic order in $MnPSe_3$. While $RuCl_3$, CrSe or FEPS are out-of-plane Ising antiferromagnets, the $MnPSe_3$ seems to be of XY type.[42]

Several factors could contribute to the observed variations in graphene resistance associated with the antiferromagnetic phase of FEPS, including: (i) different charge transfer between graphene and FEPS compared to the paramagnetic state, (ii) larger electron–phonon scattering due to the appearance of additional phonon or magnon excitations, (iii) variations in the Lorentz scattering. Further understanding of these possible scenarios can be obtained by probing the band structure of graphene through Fermi level tuning *via* a gate electrode. Transfer characteristics (I *vs.* V_g) for both pristine GFET and FEPS/GFET at different temperatures are shown in Fig. 3b and d. The bias voltage is fixed to V = 1 V. The characteristic Dirac cone-like charge transfer can be observed in both

devices. The charge neutrality point (CNP, minimum in current) at the highest measured temperature (dark red curves) appears shifted to positive $V_g \sim 33$ V in pristine graphene and $V_g \sim 41$ V in the heterostructure. The initial shift in the GFET is ascribed to p-doping due to residues from the CVD growth and the nanofabrication of the devices.[31,32] The formation of the FEPS/GFET heterostructure seems to induce a further shift toward a more positive V_g, indicating the electron acceptor nature of FEPS when in contact with graphene. This initial charge transfer is not clearly observed in the room-temperature Raman spectra (see Fig. 1d and 2), possibly due to local variations in the interlayer coupling between graphene and FEPS.[19] The presented Raman spectra represent an average of individual spectra taken at different points on the graphene surface, which may be locally, well or poorly coupled to the FEPS flake. In contrast, the observed shift in the CNP likely reflects the global variation of the electronic properties of the entire graphene monolayer involved in transport. Notably, the temperature evolution of the transfer characteristics is strikingly different for GFET and FEPS/GFET. Fig. 3b and d show the evolution of the transfer characteristics when sweeping up the temperature (ΔT = 2 K) from 90 K up to 180 K. A zoom-in around the CNP can be seen in the insets of the figures. The pristine GFET does not show any significant dependence on temperature. In contrast, a shift of the cone toward lower gate voltages (ΔCNP = −4.8 V) is triggered in the FEPS/GFET right at the Néel temperature, consistent with the reduction in p-doping observed in Raman spectroscopy. The same behaviour can be observed in device A (see Fig. S4 in the SI). This effect becomes even more evident when plotting the position of the CNP as a function of the temperature in Fig. 3c. The associated residual carrier density (n) is also shown in the axes. See Experimental section for details about the calculation. A steady drop in the residual carrier density appears around the Néel temperature and reaches $\Delta n = -1.196 \times 10^{12}$ cm^{-2} (~13.72% drop) on FEPS/GFET, in contrast to the much lower $\Delta n = -0.014 \times 10^{12}$ cm^{-2} (~0.18% drop) obtained for the GFET. The shift seems to start at somewhat higher temperatures than the Néel temperature. This is in part due to the experimental noise in the measurement. Besides, electron transport measurements may already reflect growing magnetic correlations and the starting formation of domains, close to the Néel temperature.[43] This result, together with the Raman spectroscopy, points to a distinct charge transfer between flakes in the antiferromagnetic and the paramagnetic regimes.

Finally, the current at the CNP in the FEPS/GFET does not follow the expected monotonic temperature dependence observed in the GFET. As shown in the inset in Fig. 3d, the minimum current increases as temperature decreases down to the Néel temperature of FEPS. See Fig. S5 in the SI. This trend may reflect a reduction in phonon scattering or improved interfacial coupling. However, below the Néel temperature, the current at the minimum drops sharply, consistent with a magnetism-induced modulation of charge transfer and carrier density in graphene triggered by the antiferromagnetic ordering of FEPS. All these effects are absent in the pristine GFET, supporting the interpretation that the magnetic phase transition in FEPS plays a central role in modulating the electronic properties of the heterostructure.

The interplay between conductance and magnetism in the FEPS/GFET heterostructure has been further investigated using periodic DFT calculations. First, the stability of the heterostructure has been analyzed. The geometry of the heterostructure has been optimized for four different magnetic states of the FEPS layer, the expected antiferromagnetic zigzag (AFM zigzag), antiferromagnetic Néel (AFM Néel), ferromagnetic (FM) and special quasi-random structure (SQS) paramagnetic (PM) configurations. The latter was developed by Zunger *et al.* to describe chemically disordered alloys and generalized by van de Walle *et al.* for the case of magnetic disorder.[44,45] A paramagnetic SQS (SQS PM) is a supercell which is decorated with up and down moments on the Fe atoms in such a way as to accurately reproduce the local spin–spin correlations expected in a random, dynamic paramagnet using just a single cell. See extensive details about the DFT simulations in the SI. The comparison between different magnetic models provides a deeper insight into how the magnetic texture influences the properties of the heterostructure. For clarity, the expected AFM zigzag and SQS PM configurations are presented in Fig. 4, while the AFM Néel and FM configurations are provided in Fig. S6 in the SI for the rest of the discussion. Only small changes on the Fe–Fe bond distances are observed for the deposited FEPS layer with respect to the isolated one. In all cases, the interaction with the graphene produces an enlargement of the bond distances, that should be manifested in the attenuation of the magnetic coupling among Fe centres. This effect is independent of the U value adopted in our DFT+U calculations (see Tables S2 and S3 in the SI to check results for U = 1.2 eV and U = 2.2 eV). For the FEPS monolayer, the AFM zigzag solution is the ground state, in agreement with the experimental data and previous theoretical studies.[3,28,45] It is separated by 21.4, 141.8, 191.1 meV from SQS PM, AFM Néel and FM solutions. When the FEPS/GFET heterostructure is formed, the relative energies are reduced to 18.6, 107.9, and 170.6 meV, respectively. The relative energies of the different solutions are slightly larger when U = 1.2 eV is employed, but they follow the same trend (see Table S4 in the SI). These results indicate that the magnetic interactions inside the FEPS layer are attenuated due to the presence of graphene, in line with the observed enlargement of the Fe–Fe distances. Notice that the explored SQS PM solution is closely related to the AFM zigzag one, resulting from the spin interchange of two next-nearest neighbour Fe centres.

This limited energy difference (18.6 meV) agrees with the estimated amplitude of the magnetic coupling constants inside the Fe hexagons ($|J_{ij}| \sim$ 1–6 meV).[46] Nevertheless, these two magnetic states exhibit different transport properties, as observed experimentally. Fig. 4b and Fig. S6b show the density of states for each magnetic solution for FEPS/GFET, and the projection on each component of the heterostructure.

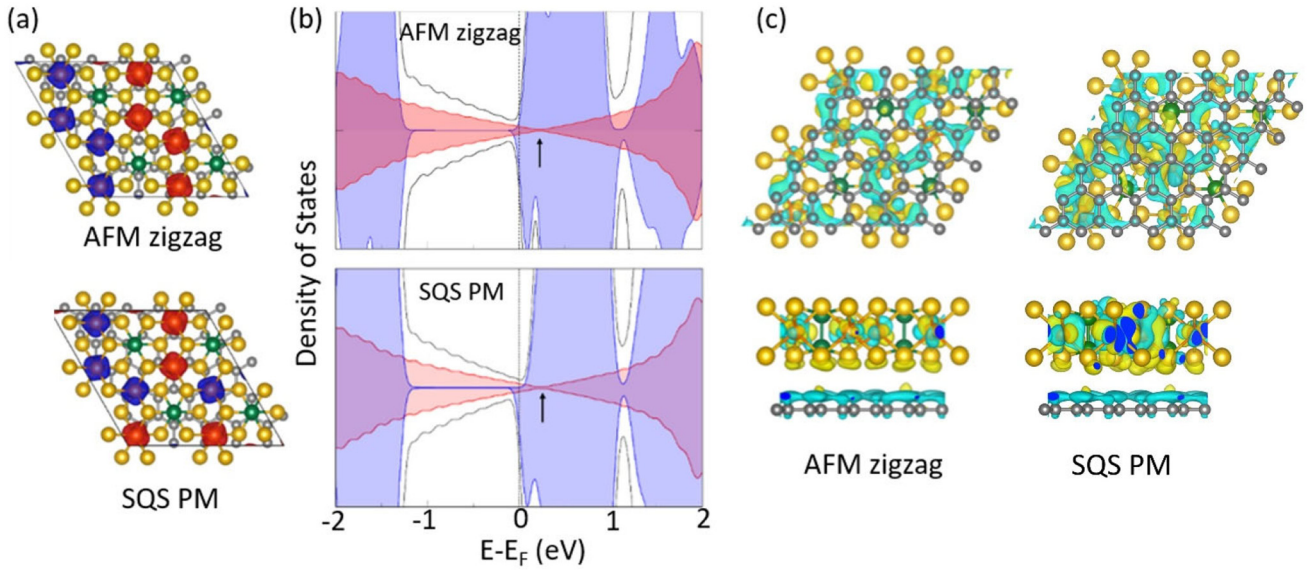

Fig. 4 (a) FEPS unit cell employed in calculations, with eight Fe centres. Gray, yellow, green and orange balls represent C, S, P, and Fe atoms, respectively. Red and blue surfaces represent the spin-up and spin-down densities of each magnetic solution, mainly localized on Fe centres (isovalue 10−2 e Å^{-3}, DFT+U calculations with U = 1.2 eV). (b) Density of states (black) close to the Fermi level, projected on graphene (red) and FEPS (blue) for AFM zigzag and SQS PM magnetic solutions. The arrow indicates the position of the graphene valence band edge. (c) Charge transfer from graphene to FEPS. Top and side views of the difference of electronic density between the heterostructure and the superposition of graphene and FEPS, $\Delta\rho$. Blue (yellow) surfaces represent regions where the electronic density decreases (increases) when the two layers interact (isovalue ~2 10−4 e Å^{-3}). For an easier analysis, note that graphene is on top of FEPS for the top view. See Fig. S6 for an equivalent figure for the AFM Néel and FM solutions.

Occupied and empty states of FEPS are separated by about 1.3 eV, in line with the experimental band gap of 1.23 eV. Interestingly, the graphene valence band edge is shifted towards the conduction band of the heterostructure, the energy shift following FM > SQS PM > AFM zigzag > AFM Néel. In other words, states occupied in pristine graphene become unoccupied in contact with FEPS. This clearly suggests a charge transfer from graphene to FEPS, whose magnitude follows the same trend as the energy shift of the valence band edge. That is, a larger charge transfer for SQS PM than for the AFM zigzag. This result is further supported by the plots of the difference of electronic density, $\Delta\rho$ ($\rho_{\mathrm{FEPS/GFET}} - (\rho_{\mathrm{graphene}} + \rho_{\mathrm{FEPS}})$, see Fig. 4c and Fig. S6c), where blue (yellow) surfaces represent regions where the electronic density decreases (increases), mainly localized around the graphene C atoms (FEPS atoms).

It is worth noticing that the interlayer distance resulting from our DFT calculations could slightly vary under different approaches modelling the vdW interactions. This could affect the extension of the charge transfer across the interface, as observed in recent studies dealing with vdW heterostructures.[47,48] However, our calculations indicate that the separation between the FEPS layer and graphene (about 3.5 Å) is independent of the magnetic state of FEPS layer.

Then it is reasonable to consider that changes due to the approach chosen to model the vdW interactions should equally affect the different FEPS magnetic states, the trends observed in our study remain meaningful.

Finally, we have simulated transport across the heterostructure for the different FEPS magnetic solutions. Fig. 5 shows the thermal dependence of the graphene resistivity in the heterostructure for different initial p-type doping concentrations that simulate initially pristine graphene (Fig. 5a) and more realistic scenarios with graphene being doped by external impurities (Fig. 5b and c and Fig. S7). The AFM Néel phase shows a unique behavior, with higher resistivity than the AFM zigzag one in all cases, indicating that a Néel phase is not a good model for the paramagnetic state (see SI). Interestingly, the graphene resistivity is higher with FEPS in AFM zigzag state than for the SQS PM state in every case, even when p-type defects are introduced in the system. This indicates that the magnetic order in FEPS, simulated here with the AFM zigzag solution, modifies the transport properties of graphene, decreasing its conductivity. These results suggest that the extension of the charge transfer from graphene to FEPS drives the change observed experimentally on the conductivity of the heterostructure. The higher the charge transfer (or, equivalently, the higher the graphene p-doping), the higher the conductivity. The interfacial charge transfer is reduced below the Néel temperature, due to the transition of FEPS to the AFM zigzag state, increasing the resistivity of the system as observed experimentally. A comparison between simulated transport and experimental resistivity can be seen in Fig. 5d. The experimental resistivity in the FEPS/GFET switches between SQS PM and AFM zigzag at the Néel temperature.

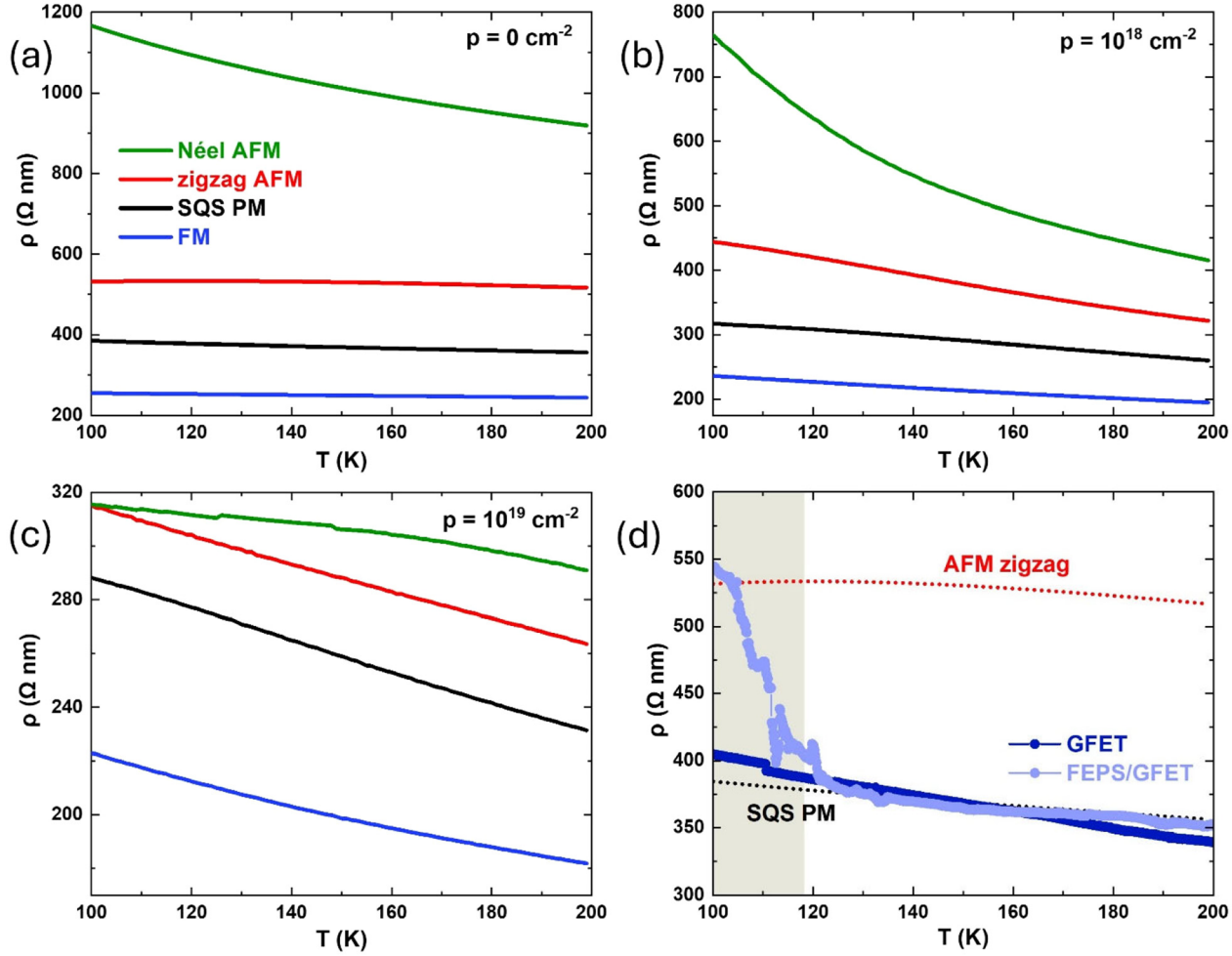

Fig. 5 (a–c) Simulated transport properties for FEPS/GFET containing different initial p-doping concentrations. The first one is analogue to the pristine graphene case. (d) Experimental resistivity of a pristine GFET (dark blue dots) and the FEPS/GFET heterostructure (device A, light blue dots) obtained from Fig. 3. The dotted lines are the simulated transport of the FEPS/GFET for the AFM zigzag and the SQS PM. The experimental resistivity switches between the two solutions at the Néel temperature.

Conclusions

In this work we show the fabrication of antiferromagnetic $FePS_3$/graphene vdW heterostructures and their implementation into a field-effect transistor. We demonstrate that the antiferromagnetic phase transition in FEPS strongly modulates the electronic properties of graphene in the heterostructure. Temperature-dependent electron transport measurements reveal a sharp increase in graphene resistance and a significant shift of the charge neutrality point at the FEPS Néel temperature. This marked reduction in the residual carrier density points to a sudden change in the interfacial charge transfer upon magnetic ordering.

Raman spectroscopy further supports this scenario through the broadening of the G and 2D bands below the Néel temperature, consistent with a reduction in graphene p-doping. DFT calculations corroborate the experimental findings, showing how the magnetic state of FEPS modifies the occupation of the valence band of graphene in FEPS/GFET. Magnetic order in the FEPS layer diminishes the charge transfer from graphene to FEPS, decreasing the p-type defects concentration in graphene, and thus increasing the resistivity of the heterostructure below Néel temperature. All in all, these findings provide compelling evidence of a magnetism-induced electronic coupling across the interface, highlighting the potential of 2D antiferromagnetic materials for gate-tunable spintronic and magnetoelectronic applications based on graphene. Future work will explore the role of an external magnetic field in tuning spin dynamics across the Néel temperature, including effects such as magnetic domain reorientation and spin canting, and how these phenomena may influence the electronic transport properties of graphene.

Experimental section

Materials

FEPS crystals with typical lateral sizes of 5 mm are commercially available from HQ Graphene.[49] Their purity (over

99.99%) is confirmed by X-ray diffraction (XRD) and energy-dispersive X-ray spectroscopy (EDX). Commercial graphene field-effect transistors were obtained from Graphenea.[50] The graphene channel size between the gold electrodes can vary. For the described experiments in this work, the dimensions of the graphene window were 50 × 30 μm (device A) and 50 × 50 μm (device B).

Fabrication of heterostructures

Exfoliated FEPS flakes are deposited onto GFETs in a transfer station (HQGraphene) equipped with an optical microscope and a set of micromanipulators. A prior annealing of the GFET (<300 °C, 2 h) is carried out in high vacuum conditions to ensure the cleanest surface possible.

Magnetic measurements

Magnetic properties of bulk and exfoliated $FePS_3$ were studied with a Quantum Design MPMS-5S SQUID magnetometer, as reported elsewhere.[41]

Structural characterization

The topography of the FEPS/GFET device was characterized by means of Scanning Force Microscopy (SFM). A Cervantes Full mode SFM system from Nanotec Electronica SL, together with PPP-FMR probes from Nanosensors, with a nominal resonance frequency of 75 kHz and spring constant of 2.8 N m^{-1}, were used to conduct the measurements in ambient conditions.[51] The measurements were carried out in dynamic amplitude modulation mode. An inertial slider was used to control the relative position of the cantilever onto the FEPS/GFET device. WSxM software was employed both for data acquisition and image processing.[52]

Temperature-dependent Raman spectra were acquired using a Bruker Senterra confocal Raman microscope (Bruker Optic, Ettlingen, Germany, resolution 3–5 cm^{-1}). Temperature was swept in a Linkam T95 with a LNP 95 Liquid Nitrogen Cooling System under N_2 atmosphere. The heating rate is set to 20 K min^{-1} in the range 90–300 K. Raman spectra were collected after a thermalization time of 5 min at every investigated temperature. The excitation was carried out using a 532 nm laser excitation beam, with a 20× long distance objective, 2 mW maximum power, 6 s acquisition time, and 10 repetitions. Each Raman spectrum results from an average of eight points on pristine GFET or FEPS/GFET heterostructure. Error bars are calculated combining the errors associated with the fitting of the individual data and the ones coming from the statistical treatment of the data.

Electron transport measurements

Electron transport measurements on pristine graphene and FEPS/GFET heterostructures were performed in a cryogenic TTPX Probe Station commercialized by LakeShore Cryotronics. Temperature was controllably swept from room temperature down to 77 K by combining a steady flow of liquid nitrogen with a PID-based Lakeshore temperature controller.

Gate voltages were applied with a TENMA source. A Keithley 2450 Sourcemeter was employed for both applying drain–source voltages and measuring drain–source current. Residual carrier density associated to every CNP value was calculated using the following equation:

$$n = \frac{C}{e}\mathrm{CNP} = \frac{\varepsilon_0 \varepsilon_r}{ed}\mathrm{CNP}$$

where e is the electron charge and C is the capacitance between silicon substrate and graphene. ε_0 and ε_r are vacuum permittivity (8.85×10^{-12} F m^{-1}) and silicon oxide relative permittivity (3.9). The thickness of the silicon oxide layer between the silicon substrate and the graphene layer is d = 90 nm. All measurements were performed in vacuum conditions (~10^{-6} mbar).

Theoretical simulations

The interaction between FEPS and graphene was studied by means of periodic DFT calculations using VASP (Vienna *ab initio* simulation package) code.[53–56] The generalized gradient approximation (GGA) is employed with the Perdew–Burke–Ernzerhof (PBE) exchange–correlation functional and projector-augmented wave (PAW) potentials.[57–59] An effective Hubbard term (U_{eff}) has been used to describe the localized 3d orbitals of Fe centres, using Dudarev approach and the van der Waals interactions are considered through the Tkatchenko–Scheffler method.[60,61] In our computational models, FEPS flakes are represented with a single layer, assuming that the impact of FEPS on graphene transport properties is mainly governed by the layer in direct contact with graphene. See SI for extensive additional details about the DFT simulations and the different magnetic models studied.

Conflicts of interest

There are no conflicts to declare.

Data availability

The data supporting this article have been included in the main manuscript or as part of the SI.

The Supplemenary Information file contains extensive details about the DFT calculations, additional experimental examples, Raman data and opitcal images of the fabrication of the heterostructure. See DOI: **https://doi.org/10.1039/d5nr02538a**.

Acknowledgements

This work has received support from grants RYC2019-028429-I (EB), CNS2024-154501 (EB) TED2021-130957B-C55 (EB, MJ, EC), PID2022-140923NB-C22 (EB, AG-M), PID2021-122980OA-C53(MJ) funded by MCIN/AEI/10.13039/501100011033 and the MAD2D-CM-MRR MATERIALES AVANZADOS-IMDEA NC-4 (JSC, SG). C. J. C., R. S. A. and N. M. P. acknowledge the financial support through grant PID2021-127674NB-I00 funded by MICIU/AEI/10.13039/

501100011033/FEDER/UE. The technical support of the Supercomputing Team of the Centro Informático Científico de Andalucía (CICA) and Cenits-COMPUTAEX (Extremadura, Spain) are also acknowledged.

References

1 N. D. Mermin and H. Wagner, *Phys. Rev. Lett.*, 1966, **17**, 1133–1136.
2 R. J. Birgeneau, H. J. Guggenheim and G. Shirane, *Phys. Rev. Lett.*, 1969, **22**, 720–723.
3 J.-U. Lee, S. Lee, J. H. Ryoo, S. Kang, T. Y. Kim, P. Kim, C.-H. Park, J.-G. Park and H. Cheong, *Nano Lett.*, 2016, **16**, 7433–7438.
4 X. Wang, K. Du, Y. Y. Fredrik Liu, P. Hu, J. Zhang, Q. Zhang, M. H. S. Owen, X. Lu, C. K. Gan, P. Sengupta, C. Kloc and Q. Xiong, *2D Mater.*, 2016, **3**, 031009.
5 B. Huang, G. Clark, E. Navarro-Moratalla, D. R. Klein, R. Cheng, K. L. Seyler, D. Zhong, E. Schmidgall, M. A. McGuire, D. H. Cobden, W. Yao, D. Xiao, P. Jarillo-Herrero and X. Xu, *Nature*, 2017, **546**, 270–273.
6 C. Gong, L. Li, Z. Li, H. Ji, A. Stern, Y. Xia, T. Cao, W. Bao, C. Wang, Y. Wang, Z. Q. Qiu, R. J. Cava, S. G. Louie, J. Xia and X. Zhang, *Nature*, 2017, **546**, 265–269.
7 S. Jiang, L. Li, Z. Wang, K. F. Mak and J. Shan, *Nat. Nanotechnol.*, 2018, **13**, 549–553.
8 Y. Deng, Y. Yu, Y. Song, J. Zhang, N. Z. Wang, Z. Sun, Y. Yi, Y. Z. Wu, S. Wu, J. Zhu, J. Wang, X. H. Chen and Y. Zhang, *Nature*, 2018, **563**, 94–99.
9 W. Chen, Z. Sun, Z. Wang, L. Gu, X. Xu, S. Wu and C. Gao, *Science*, 2019, **366**, 983–987.
10 A. Chakraborty, A. K. Srivastava, A. K. Sharma, A. K. Gopi, K. Mohseni, A. Ernst, H. Deniz, B. K. Hazra, S. Das, P. Sessi, I. Kostanovskiy, T. Ma, H. L. Meyerheim and S. S. P. Parkin, *Adv. Mater.*, 2022, **34**, 2108637.
11 T. Song, Q.-C. Sun, E. Anderson, C. Wang, J. Qian, T. Taniguchi, K. Watanabe, M. A. McGuire, R. St hr, D. Xiao, T. Cao, J. Wrachtrup and X. Xu, *Science*, 2021, **374**, 1140–1144.
12 X. Chen, C. Zheng and Y. Liu, *Magnetochemistry*, 2024, **10**, 50.
13 C. Gong and X. Zhang, *Science*, 2019, **363**, eaav4450.
14 C. Broholm, R. J. Cava, S. A. Kivelson, D. G. Nocera, M. R. Norman and T. Senthil, *Science*, 2020, **367**, eaay0668.
15 M. Gibertini, M. Koperski, A. F. Morpurgo and K. S. Novoselov, *Nat. Nanotechnol.*, 2019, **14**, 408–419.
16 Y. Zhang, W. Wang, M. Huang, P. Liu, G. Hu, C. Feng, X. Lei, M. Gu, H. Yang, K. Liu, B. Xiang and Y. Lu, *Nanoscale*, 2020, **12**, 23266–23273.
17 Y. Wu, G. Yin, L. Pan, A. J. Grutter, Q. Pan, A. Lee, D. A. Gilbert, J. A. Borchers, W. Ratcliff, A. Li, X.-D. Han and K. L. Wang, *Nat. Electron.*, 2020, **3**, 604–611.
18 Y. Wang, X. Gao, K. Yang, P. Gu, X. Lu, S. Zhang, Y. Gao, N. Ren, B. Dong, Y. Jiang, K. Watanabe, T. Taniguchi, J. Kang, W. Lou, J. Mao, J. Liu, Y. Ye, Z. Han, K. Chang, J. Zhang and Z. Zhang, *Nat. Nanotechnol.*, 2022, **17**, 1272–1279.
19 B. Zhou, J. Balgley, P. Lampen-Kelley, J. Q. Yan, D. G. Mandrus and E. A. Henriksen, *Phys. Rev. B*, 2019, **100**, 165426.
20 S. K. Chakraborty, B. Kundu, B. Nayak, S. P. Dash and P. K. Sahoo, *iScience*, 2022, **25**, 103942.
21 C.-C. Tseng, T. Song, Q. Jiang, Z. Lin, C. Wang, J. Suh, K. Watanabe, T. Taniguchi, M. A. McGuire, D. Xiao, J.-H. Chu, D. H. Cobden, X. Xu and M. Yankowitz, *Nano Lett.*, 2022, **22**, 8495–8501.
22 S. Mashhadi, Y. Kim, J. Kim, D. Weber, T. Taniguchi, K. Watanabe, N. Park, B. Lotsch, J. H. Smet, M. Burghard and K. Kern, *Nano Lett.*, 2019, **19**, 4659–4665.
23 X. Yi, Q. Chen, K. Wang, Y. Yu, Y. Yan, X. Jiang, C. Yan and S. Wang, *Phys. Rev. B*, 2023, **108**, 125427.
24 M. Ramos, F. Carrascoso, R. Frisenda, P. Gant, S. Mañas-Valero, D. L. Esteras, J. J. Baldoví, E. Coronado, A. Castellanos-Gomez and M. R. Calvo, *npj 2D Mater. Appl.*, 2021, **5**, 19.
25 S. Liu, A. Granados del Águila, D. Bhowmick, C. K. Gan, T. Thu Ha Do, M. A. Prosnikov, D. Sedmidubsk, Z. Sofer, P. C. M. Christianen, P. Sengupta and Q. Xiong, *Phys. Rev. Lett.*, 2021, **127**, 097401.
26 B. Ilyas, T. Luo, A. von Hoegen, E. Viñas Boström, Z. Zhang, J. Park, J. Kim, J.-G. Park, K. A. Nelson, A. Rubio and N. Gedik, *Nature*, 2024, **636**, 609–614.
27 S. Maity, S. Das, M. Palit, K. Dey, B. Das, T. Kundu, R. Paramanik, B. K. De, H. S. Kunwar and S. Datta, *arXiv*, arXiv:2411.08597, (accessed June 13, 2025).
28 M. Amirabbasi and P. Kratzer, *Phys. Rev. B*, 2023, **107**, 024401.
29 S. Puebla, H. Li, H. Zhang and A. Castellanos-Gomez, *Adv. Photonics Res.*, 2022, **3**, 2100221.
30 W. Zhang, Q. Zhao, S. Puebla, T. Wang, R. Frisenda and A. Castellanos-Gomez, *Mater. Today Adv.*, 2021, **10**, 100143.
31 M. Kalbac, A. Reina-Cecco, H. Farhat, J. Kong, L. Kavan and M. S. Dresselhaus, *ACS Nano*, 2010, **4**, 6055–6063.
32 M. Vázquez Sulleiro, A. Develioglu, R. Quirós-Ovies, L. Martín-Pérez, N. Martín Sabanés, M. L. Gonzalez-Juarez, I. J. Gómez, M. Vera-Hidalgo, V. Sebastián, J. Santamaría, E. Burzurí and E. M. Pérez, *Nat. Chem.*, 2022, **14**, 695–700.
33 A. Das, S. Pisana, B. Chakraborty, S. Piscanec, S. K. Saha, U. V. Waghmare, K. S. Novoselov, H. R. Krishnamurthy, A. K. Geim, A. C. Ferrari and A. K. Sood, *Nat. Nanotechnol.*, 2008, **3**, 210–215.
34 J.-B. Wu, M.-L. Lin, X. Cong, H.-N. Liu and P.-H. Tan, *Chem. Soc. Rev.*, 2018, **47**, 1822–1873.
35 D. J. Late, U. Maitra, L. S. Panchakarla, U. V. Waghmare and C. N. R. Rao, *J. Phys.: Condens. Matter*, 2011, **23**, 055303.
36 J. Yan, Y. Zhang, P. Kim and A. Pinczuk, *Phys. Rev. Lett.*, 2007, **98**, 166802.
37 C. Casiraghi, *Phys. Status Solidi RRL*, 2009, **3**, 175–177.
38 S. Berciaud, X. Li, H. Htoon, L. E. Brus, S. K. Doorn and T. F. Heinz, *Nano Lett.*, 2013, **13**, 3517–3523.

39 J.-H. Chen, C. Jang, S. Xiao, M. Ishigami and M. S. Fuhrer, *Nat. Nanotechnol.*, 2008, **3**, 206–209.
40 K. Ichimura and M. Sano, *Synth. Met.*, 1991, **45**, 203–211.
41 L. Martín-Pérez, S. Medina Rivero, M. Vázquez Sulleiro, A. Naranjo, I. J. Gómez, M. L. Ruíz-González, A. Castellanos-Gomez, M. Garcia-Hernandez, E. M. Pérez and E. Burzurí, *ACS Nano*, 2023, **17**, 3007–3018.
42 J.-T. Yang, C.-J. Xu, H.-J. Wang, Q. Min, S.-J. Luo, Y.-C. Xiong, W. Ren and C. Jing, *J. Phys.: Condens. Matter*, 2023, **35**, 395501.
43 K. Kim, S. Y. Lim, J. Kim, J.-U. Lee, S. Lee, P. Kim, K. Park, S. Son, C.-H. Park, J.-G. Park and H. Cheong, *2D Mater.*, 2019, **6**, 041001.
44 A. Zunger, S. H. Wei, L. G. Ferreira and J. E. Bernard, *Phys. Rev. Lett.*, 1990, **65**, 353–356.
45 A. van de Walle, P. Tiwary, M. de Jong, D. L. Olmsted, M. Asta, A. Dick, D. Shin, Y. Wang, L. Q. Chen and Z. K. Liu, *CALPHAD: Comput. Coupling Phase Diagrams Thermochem.*, 2013, **42**, 13–18.
46 B. Pestka, J. Strasdas, G. Bihlmayer, A. K. Budniak, M. Liebmann, N. Leuth, H. Boban, V. Feyer, I. Cojocariu, D. Baranowski, S. Mearini, Y. Amouyal, L. Waldecker, B. Beschoten, C. Stampfer, L. Plucinski, E. Lifshitz, P. Kratzer and M. Morgenstern, *ACS Nano*, 2024, **18**, 32924–32931.
47 L. Cao, X. Deng, G. Zhou, S.-J. Liang, C. V. Nguyen, L. K. Ang and Y. S. Ang, *Phys. Rev. B*, 2022, **105**, 165302.
48 C. V. Nguyen, P. T. Truong, H. V. Phuc, C. Q. Nguyen, N. T. Hiep and N. N. Hieu, *Nano Lett.*, 2025, **25**, 10673–10679.
49 *HQ Graphene*, $FePS_3$, **https://www.hqgraphene.com/FePS3.php**, (accessed June 13, 2025).
50 *Graphenea*, GFET-S10 for sensing applications, **https://www.graphenea.com/products/gfet-s10-for-sensing-applications-10-mm-x-10-mm**, (accessed June 13, 2025).
51 *Nanosensors*, NANOSENSORS™ AFM Tips·Research Driven Excellence Since 1990, (accessed June 13, 2025).
52 I. Horcas, R. Fernández, J. M. Gómez-Rodríguez, J. Colchero, J. Gómez-Herrero and A. M. Baro, *Rev. Sci. Instrum.*, 2007, **78**, 013705.
53 G. Kresse and J. Furthmüller, *Comput. Mater. Sci.*, 1996, **6**, 15–50.
54 G. Kresse and J. Furthmüller, *Phys. Rev. B: Condens. Matter Mater. Phys.*, 1996, **54**, 11169–11186.
55 G. Kresse and J. Hafner, *Phys. Rev. B: Condens. Matter Mater. Phys.*, 1994, **49**, 14251–14269.
56 G. Kresse and J. Hafner, *Phys. Rev. B: Condens. Matter Mater. Phys.*, 1993, **47**, 558–561.
57 J. P. Perdew, K. Burke and M. Ernzerhof, *Phys. Rev. Lett.*, 1996, **77**, 3865–3868.
58 P. E. Blöchl, *Phys. Rev. B: Condens. Matter Mater. Phys.*, 1994, **50**, 17953–17979.
59 G. Kresse and D. Joubert, *Phys. Rev. B: Condens. Matter Mater. Phys.*, 1999, **59**, 1758–1775.
60 S. L. Dudarev, G. A. Botton, S. Y. Savrasov, C. J. Humphreys and A. P. Sutton, *Phys. Rev. B: Condens. Matter Mater. Phys.*, 1998, **57**, 1505–1509.
61 A. Tkatchenko and M. Scheffler, *Phys. Rev. Lett.*, 2009, **102**, 073005.